Dalton Transactions

ROYAL SOCIETY OF CHEMISTRY

PAPER

View Article Online
View Journal | View Issue

Cite this: *Dalton Trans.*, 2023, **52**, 15775

Surface ligand length influences kinetics of H-atom uptake in polyoxovanadate-alkoxide clusters†

Chari Y. M. Peter, Eric Schreiber, Kathryn R. Proe and Ellen M. Matson *

The uptake of hydrogen atoms (H-atoms) at reducible metal oxide nanocrystal surfaces has implications in catalysis and energy storage. However, it is often difficult to gain insight into the physicochemical factors that dictate the thermodynamics and kinetics of H-atom transfer to the surface of these assemblies. Recently, our research group has demonstrated the formation of oxygen-atom (O-atom) defects in polyoxovanadate-alkoxide (POV-alkoxide) clusters *via* conversion of surface oxido moieties to aquo ligands, which can be accomplished *via* addition of two H-atom equivalents. Here, we present the dependence of O-atom defect formation *via* H-atom transfer at the surface of vanadium oxide clusters on the length of surface alkoxide ligands. Analysis of H-atom transfer reactions to low-valent POV-alkoxide clusters $[V_6O_7(OR)_{12}]^{1-}$ (R = Me, Et, ^{n}Pr, ^{n}Bu) reveals that the length of primary alkoxide surface ligands does not significantly influence the thermodynamics of these processes. However, surface ligand length has a significant impact on the kinetics of these PCET reactions. Indeed, the methoxide-bridged cluster, $[V_6O_7(OMe)_{12}]^{1-}$ reacts ~20 times faster than the other derivatives evaluated. Interestingly, as the aliphatic linkages are increased in size from $-C_2H_5$ to $-C_4H_9$, reaction rates remain consistent, suggesting restricted access to available ligand conformers as a result of the incompatibility of the aliphatic ligands and acetonitrile may buffer further changes to the rate of reaction.

Received 2nd July 2023,
Accepted 21st September 2023

DOI: 10.1039/d3dt02074f

rsc.li/dalton

Introduction

Colloidal, nanocrystalline reducible metal oxides are an important class of materials with relevance in emergent energy storage and conversion technologies.[1–3] Nanoparticles possess high surface-to-volume ratios, increasing the importance of surface structure in the electronic properties and reactivity of the material.[4–6] Accordingly, an important consideration in controlling the properties of nanocrystalline materials is the identity of surface ligands. Ligands are organic molecules which bind to the surface of a metal oxide and are responsible for controlling particle size, structure, and colloidal stability.[7,8] Ligands also influence the reactivity of nanocrystals by controlling access of small molecule substrates to surface sites of the material.[9–12] Unfortunately, the lack of mono-dispersity in ligand substitution at colloid surfaces renders explicit investigation of structure–function relationships related to ligand identity/density and the reactivity of the nanoscopic assembly challenging.

Over the past decade, colloidal redox active metal oxides have been receiving increased attention for their utility in proton-coupled electron transfer (PCET) reactivity.[13,14] The uptake and transfer of hydrogen atom (H-atom) equivalents at the surface of nanomaterials has positioned them to be effective redox catalysts and mediators for small molecule (de) hydrogenation reactions.[15,16] However, the influence of surface ligands on these processes, such as reactive site accessibility, driving force, and reaction kinetics, remain underexplored due to the aforementioned challenges associated with the uniform modification of the ligand shell surrounding a nanomaterial. Thus, the employment of molecular model complexes may provide useful insights into how the sterics of the ligand shell influences net H-atom transfer reactions at material surfaces.

Polyoxometalates have long been cited as models for reducible metal oxide materials.[17–21] With relevance to the current study, variations of these metal oxide clusters can be generated in organic–inorganic hybrid form. Organo-functionalization is often accomplished post-synthetically; manipulation of the cluster structure in the presence of base exposes a single face of nucleophilic bridging oxide moieties, which upon ligand substitution results in the formation of Janus-type cluster complexes.[22–25] Uniform ligand substitution in polyoxotungstates and polyoxomolybdates has not been observed, as the acidity of the cluster surface renders the majority of surface oxygen atoms non-reactive. In contrast, many organofunctionalized polyoxovanadates (POVs) have been reported, with a

Department of Chemistry, University of Rochester, Rochester, NY 14627, USA.
E-mail: matson@chem.rochester.edu

† Electronic supplementary information (ESI) available. See DOI: https://doi.org/10.1039/d3dt02074f

range of ligand substitution patterns.[26] This unique property of POVs is credited to the increased basicity of vanadium ions in comparison to Group VI metals.[27,28] Bridging ligands in these systems stabilize a range of accessible metal oxidation states, and provide topological and subsurface structures that resemble ligand-capped nanomaterials (Fig. 1).[26] Taken together, these complexes provide an intriguing scaffold for studying redox processes at ligand-capped nanocrystalline oxide surfaces with atomic precision.

Our research team is studying PCET at polyoxovanadate-alkoxide (POV-alkoxide) clusters in an effort to gain atomic insight into charge compensation at nanomaterial surfaces (Fig. 1).[21,29,30] We have found that ligand density influences the regioselectivity of PCET, with complexes featuring unfunctionalized bridging oxides forming μ_2-OH moieties, and organic-saturated complexes undergoing O-atom vacancy formation, presumably *via* sequential H-atom addition to a terminal oxide ligand (see mechanism outlined in Scheme 1). This reactivity is a consequence of the high ligand density on the cluster surface; saturation of nucleophilic bridging oxide sites limits the reactivity of H-atom equivalents to the terminal oxo moieties at the surface of the assembly.

The investigation of POV-alkoxide clusters provides further opportunities to explore the influence of ligand substitution on the reactivity of the core. Prior work from our laboratory has described the synthesis of a series of Lindqvist-type POV-alkoxide clusters featuring bridging alkoxide ligands with varying carbon-chain length.[31,32] The overall electronic consequences of changing the surface functionalities are small; all reported cyclic voltammograms for the series of organo-substituted POV-alkoxide clusters are analogous. However, ligand identity has been shown to play a role in mediating reactivity and charge compensation processes. For example, O-atom vacancy formation at the surface of POV-alkoxide clusters *via* O-atom transfer to phosphines (PR_3) occurs readily for the methoxide-functionalized assembly, whereas the same reaction is inhibited in the case of $[V_6O_7(O^nPr)_{12}]$.[33] Similarly, the uptake of alkali ions at the surface of POV-alkoxide clusters has been demonstrated to be sensitive to the ligand shell; longer primary alkoxide chains tune the thermodynamics of lithium binding by altering compatibility of the ligand sphere with cations in polar solvation environments.[34,35] Thus, despite analogous core structures and electrochemical properties between POV-alkoxide derivatives, surface ligands appear to be intimately involved in the reactivity of these assemblies.

Here, we describe a systematic investigation on the uptake of e^-/H^+ pairs at the surface of POV-alkoxides bearing methoxide, ethoxide, *n*-propoxide and *n*-butoxide ligands,

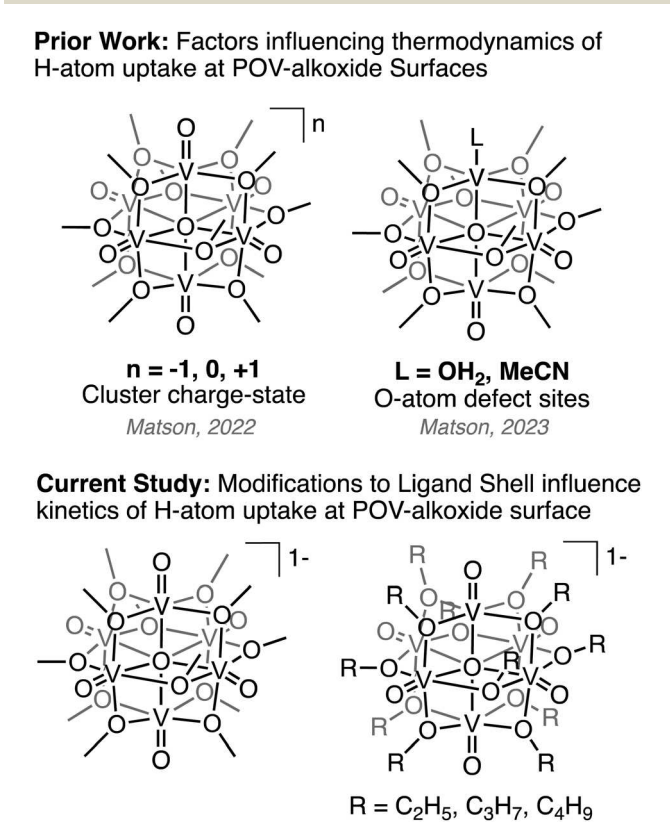

Fig. 1 Structural modifications to POV-alkoxide clusters studied by the Matson Laboratory for insight into design criteria impacting the *thermodynamics* of H-atom uptake at terminal oxo moieties (top); series of clusters studied in this work probing the impact of modifying the *n*-alkoxide ligand length on the kinetics of H-atom uptake at POV-alkoxide surface (bottom).

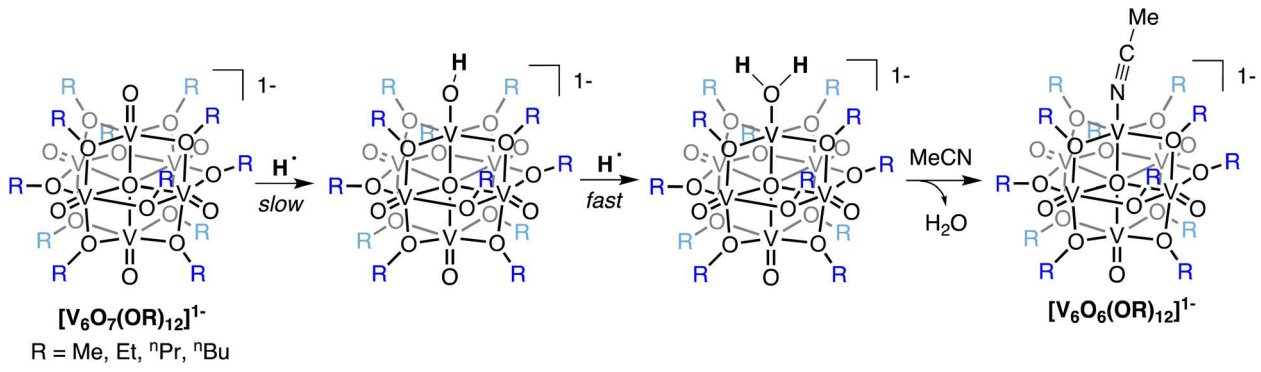

Scheme 1 Mechanism of hydrogen-atom uptake of POV-alkoxide clusters for O-atom defect formation.

$[V_6O_7(OR)_{12}]^{1-}$ (R = Me, Et, ^{n}Pr, ^{n}Bu). O-atom vacancy formation is possible in all four systems *via* net H-atom uptake at the cluster surface. The previously reported indifference of cluster core electronics to ligand identity (length) results in similar affinities of the surface of the assembly for H-atoms, as determined through the measurement of bond dissociation free energies (BDFEs) for terminal O–H bonds of the aquo adducts of the reduced species. Despite the analogous thermodynamics describing H-atom uptake at the POV-alkoxide, the kinetics of PCET to the surface of the three clusters are greatly influenced by the length of the aliphatic moieties of the ligand shell. Accelerated reaction rates of defect formation are observed in the case of the methoxide-substituted assembly in comparison to the longer-chain POV-alkoxide clusters. Steric effects are also reflected in the activation parameters of PCET, where reduction of clusters with longer alkyl groups was found to feature greater activation enthalpy and lower magnitudes of activation entropy. These results indicate that by altering ligand sterics at the surface of metal oxide systems, one can decouple driving force and kinetics, providing design cues for PCET-active nanomaterials with tailored reactivity.

Experimental section

General considerations

All manipulations were carried out in the absence of water and oxygen using standard Schlenk techniques or in a UniLab MBraun inert atmosphere drybox under a dinitrogen atmosphere. All glassware was oven-dried for a minimum of 4 h and cooled in an evacuated antechamber prior to use in the drybox. Solvents were dried and deoxygenated on a glass contour system (Pure Process Technology, LLC) and stored over 3 Å molecular sieves purchased from Fisher Scientific and activated prior to use. Hydrazobenzene, $[^nBu_4N][BH_4]$, $[^nOct_4N][OH]$ (20% MeOH solution), and 5,10-phenazine were purchased from Millipore Sigma and used as received. POV-alkoxide clusters $[^nBu_4N][V_6O_7(OR)_{12}]$ (R = CH_3),[36] and $[V_6O_7(OR)]^0$ (R = CH_3,[36] C_2H_5,[36] $^nC_3H_7$,[31] $^nC_4H_9$ [31]) were prepared according to previously reported procedures. 5,10-dihydrophenazine[37] and 5,10-dihydrophenazine-d_2 [38] were generated following literature precedent.

^{1}H NMR spectra were recorded at 400 MHz or 500 MHz on a Bruker DPX-400 or Bruker DPX-500 spectrometer, respectively, locked on the signal of deuterated solvents.[39] All chemical shifts were reported relative to the peak of the residual H signal in deuterated solvents. CD_3CN was purchased from Cambridge Isotope Laboratories, degassed by three freeze–pump–thaw cycles, and stored over fully activated 3 Å molecular sieves. THF-d_8 was purchased from Cambridge Isotope Labs in glass ampules, brought into the drybox, and stored for a period of three days over 3 Å molecular sieves prior to use.

Electronic absorption spectroscopy (UV-Vis-NIR) was collected using an Agilent Cary 6000i spectrophotometer at room temperature. Samples were prepared in the drybox in MeCN and added to air-free cuvettes and sealed prior to removing from the drybox. Kinetic experiments were carried out on an Agilient Cary 60 UV-Vis spectrophotometer held at desired temperatures using an Unisoku CoolSpek UV cryostat, as well as an Agilent Cary 3500 UV-Vis spectrophotometer held at desired temperatures with an integrated Peltier temperature control system. Mass spectrometry analyses were performed on an Advion Expression^L Compact mass spectrometer equipped with an electrospray probe and an ion-trap mass analyser (instrument error: ±0.1 amu). Direct injection analysis was employed in all cases with a sample solution in MeCN. Elemental analyses were performed on a PerkinElmer 2400 Series II Analyzer, at the CENTC Elemental Analysis Facility, University of Rochester.

Synthesis of $[^nOct_4N][V_6O_7(OCH_3)_{12}]$. A 20 mL scintillation vial was charged with $[V_6O_7(OCH_3)_{12}]^0$ (0.070 g, 0.089 mmol, 1 equiv.), a stir bar, and 8 mL of MeCN. While stirring, tetraoctylammonium hydroxide ($[^nOct_4N][OH]$) solution (20% in MeOH) (236 μL, 0.098 mmol, 1.1 equiv.) was added dropwise to the cluster solution. The reaction was stirred at 50 °C for 2 h, then the solvent was removed under reduced pressure. Characterization of the product was consistent with 1e$^-$ reduction of the cluster (0.106 g, 0.084 mmol, 94%; Fig. S1 and S2†).[40] ^{1}H NMR (500 MHz, CD_3CN, 21 °C): δ = 23.34, 3.05, 1.32, 0.90 ppm. UV-Vis-NIR (21 °C, THF): $\lambda(\varepsilon)$ = 387 nm (3612 M^{-1} cm^{-1}), 1293 nm (937 M^{-1} cm^{-1}). Elemental analysis: calc. for $C_{44}H_{104}NV_6O_{19}\cdot 3/4\ CH_2Cl_2$ (M_W = 1320.65 g mol^{-1}): C, 40.70; H, 8.05; N, 1.06. Found: C, 40.74; H, 7.93; N: 0.92.

Synthesis of $[^nBu_4N][V_6O_7(OR)_{12}]$ (R = C_2H_5, 1-ethyl; C_3H_7, 1-propyl; C_4H_9, 1-butyl). A 20 mL scintillation vial was charged with $[V_6O_7(OR)_{12}]^0$, a stir bar, and 8 mL of MeCN. In a separate vial, 1 equivalent of $[^nBu_4N][BH_4]$ was dissolved in 4 mL of MeCN. The reductant solution was added to the cluster containing vial, the vial was sealed, and the mixture was stirred at 70 °C for 2 h. During this time, the suspensions of $[V_6O_7(OC_2H_5)_{12}]^0$ and $[V_6O_7(OC_3H_7)_{12}]^0$ were observed to become homogenous. In the case of $[V_6O_7(OC_4H_9)_{12}]^0$, given the fact that the starting cluster is quite soluble in MeCN, no changes to solution homogeneity or colour were observed. For $[^nBu_4N][V_6O_7(OC_2H_5)_{12}]$ (**1-ethyl**), volatiles were removed under reduced pressure and the solid was washed with diethyl ether (3 × 10 mL). The washes were filtered, and the precipitate was extracted in MeCN and dried under reduced pressure to produce **1-ethyl** as a green solid. For **1-propyl** and **1-butyl**, after drying the crude reaction mixture under reduced pressure, the product was extracted into diethyl ether, filtered, and dried under reduced pressure to produce the corresponding cluster as a green oily solid.

$[^nBu_4N][V_6O_7(OC_2H_5)_{12}]$ (1-ethyl). $[V_6O_7(OC_2H_5)_{12}]^0$ (0.105 g, 0.11 mmol), $[^nBu_4N][BH_4]$ (0.028 g, 0.11 mmol, 1 equiv.) Yield: 0.0976 g, 0.081 mmol, 74%. All analytical data matched characterization reported previously by our group.[41]

$[^nBu_4N][V_6O_7(OC_3H_7)_{12}]$ (1-propyl). $[V_6O_7(OC_3H_7)_{12}]^0$ (0.0415 g, 0.03683 mmol), $[^nBu_4N][BH_4]$ (0.010 g, 0.036 mmol, 1 equiv.). Yield: 0.038 g, 0.028 mmol, 76%. Characterization of the product was consistent with analytical data reported previously by our group.[35]

[^{n}Bu$_4$N][V$_6$O$_7$(OC$_4$H$_9$)$_{12}$] (1-butyl). [V$_6$O$_7$(OC$_4$H$_9$)$_{12}$]^0 (0.115 g, 0.089 mmol), [^{n}Bu$_4$N][BH$_4$] (0.023 g, 0.089 mmol, 1 equiv.) Yield: 0.100 g, 0.065 mmol, 73%. We note that consistent with prior work, the ESI-MS of **1-butyl** indicates the presence of a fraction of product with some bridging-alkoxide positions occupied by methoxide substituents, with the generic formula [^{n}Bu$_4$N][V$_6$O$_7$(OC$_4$H$_9$)$_{12-x}$(OCH$_3$)$_x$] (x = 1–4; Fig. S3†). ^{1}H NMR (400 MHz, CD$_3$CN, 21 °C): δ = 25.97, 3.07, 1.60, 1.35, 0.97 ppm. Elemental analysis: calc. for C$_{64}$H$_{144}$NV$_6$O$_{19}$·NCCH$_3$ (M_W = 1537.49 g mol^{-1}): C, 50.22; H, 9.39; N, 1.77. Found: C, 49.99; H, 9.66; N: 1.77.

Synthesis of [^{n}Bu$_4$N][V$_6$O$_6$(MeCN)(OC$_2$H$_5$)$_{12}$] (2-ethyl). A 20 mL scintillation vial was charged with **1-ethyl** (0.050 g, 0.042 mmol), a stir bar, and 6 mL of MeCN. In a separate vial, 1 equiv. of 5,10-dihydrophenazine (0.008 g, 0.044 mmol) was dissolved in 4 mL of MeCN. The second solution was added dropwise to the cluster solution with vigorous stirring. The reaction solution was stirred for 1 h, over which time the colour changed from green to red-pink. The solvent was removed under reduced pressure, leaving a red-brown residue. The crude reaction mixture was washed with diethyl ether (3 × 10 mL) and filtered over a bed of Celite. The remaining solid was extracted in MeCN and dried *in vacuo* to yield [^{n}Bu$_4$N][V$_6$O$_6$(MeCN)(OC$_2$H$_5$)$_{12}$] (**2-ethyl**) (0.055 g, 0.052 mmol, 95%). Characterization of the product matched with a previous report.[41]

Synthesis of [^{n}Bu$_4$N][V$_6$O$_6$(MeCN)(OC$_3$H$_7$)$_{12}$] (2-propyl). A 20 mL scintillation vial was charged with **1-propyl** (0.050 g, 0.037 mmol), acetonitrile (6 mL) and a stir bar. In a separate vial, 1 equiv. of 5,10-dihydrophenazine (0.010 g, 0.038 mmol) was dissolved in acetonitrile (4 mL). The solution of reductant was added dropwise to the cluster-containing solution with vigorous stirring. The reaction solution was stirred for 1.5 h at room temperature, over which time the colour changed from green to brown. The solvent was removed under reduced pressure, leaving a brown residue. The crude reaction mixture was washed with diethyl ether (3 × 10 mL), then a 10 : 1 mixture of pentane and dichloromethane (2 × 11 mL), respectively and filtered over a bed of Celite. The remaining solid was extracted in acetonitrile and dried *in vacuo* to yield [^{n}Bu$_4$N][V$_6$O$_6$(MeCN)(OC$_3$H$_7$)$_{12}$] (**2-propyl**) (0.038 g, 0.028 mmol, 76%). ^{1}H NMR (500 MHz, CD$_3$CN) δ = 29.67, 28.89, −0.66, −2.18, −24.88 ppm. UV-Vis-NIR (21 °C, CH$_3$CN): $\lambda(\varepsilon)$ = 550 nm (154 M^{-1} cm^{-1}), 1038 nm (184 M^{-1} cm^{-1}). Elemental analysis: calc. for C$_{54}$H$_{123}$N$_2$V$_6$O$_{18}$·1.5 CH$_2$Cl$_2$, (M_W = 1521.61 g mol^{-1}): C, 43.81; H, 8.35; N, 1.84. Found: C, 43.52; H, 8.19; N: 1.97.

Synthesis of [^{n}Bu$_4$N][V$_6$O$_6$(MeCN)(OC$_4$H$_9$)$_{12}$] (2-butyl). A 20 mL scintillation vial was charged with **1-butyl** (0.048 g, 0.031 mmol), a stir bar, and 6 mL of MeCN. In a separate vial, 1.5 equiv. of 5,10-dihydrophenazine (0.009 g, 0.049 mmol) was dissolved in 4 mL of MeCN. The reductant solution was added dropwise to the cluster solution with vigorous stirring. The reaction solution was stirred at 25 °C for 2 h, over which time the colour changed from green to gold-brown. The solvent was removed under reduced pressure, leaving a maroon-brown residue. The crude reaction mixture was washed with a mixture of diethyl ether and pentane (1 : 1 ratio; 3 × 11 mL) and filtered over a bed of Celite. The remaining solid was extracted in MeCN and dried *in vacuo* to yield [^{n}Bu$_4$N][V$_6$O$_6$(MeCN)(OC$_4$H$_9$)$_{11}$(OCH$_3$)] (**2-butyl**) (0.020 g, 0.0135 mmol, 44%). ^{1}H NMR (500 MHz, CD$_3$CN) δ = 29.90, 29.0, −18.23, and −25.32 ppm. UV-Vis/NIR (CH$_3$CN, 21 °C) λ = 535 nm (ε = 145 M^{-1} cm^{-1}), 655 nm (ε = 60 M^{-1} cm^{-1}). Elemental analysis: calc. for C$_{58}$H$_{132}$NV$_6$O$_{18}$ (M_W = 1498.39 g mol^{-1}): C, 48.75; H, 9.2; N, 1.89. Found: C, 48.62; H, 8.99; N: 2.25.

General procedure for thermochemical analysis of the BDFE (O–H)$_{avg}$ of [V$_6$O$_6$(OH$_2$)(OR)$_{12}$]$^{1-}$

Determination of the BDFE(O–H)$_{avg}$ of [V$_6$O$_6$(OH$_2$)(OR)$_{12}$]$^{1-}$ was performed using reactions between [V$_6$O$_7$(OR)$_{12}$]$^{1-}$ and hydrazobenzene (Hydz) in THF-d_8. To ensure product solubility, the tetraoctylammonium salt of **1-methyl** was used. Equimolar amounts of cluster and reductant were measured from stock solutions in THF-d_8, loaded into a J-Young tube, and sealed prior to removal from the glovebox for analysis. Reactions were allowed to react over 7 days at room temperature, tracking progress by ^{1}H NMR spectroscopy. At this time, the relative concentrations of azobenzene (Azo) to Hydz were determined by using the integrations of resonances corresponding with each compound and normalizing for the number of protons each signal represents (Tables S1–S4†). Upon determination of [Hydz]/[Azo], the adjusted BDFE of the reductant was determined for each reaction using eqn (1) (*vide infra*), where BDFE$_{Hydz}$ = 60.4 kcal mol^{-1} and n = 2. Calculations are tabulated in Tables S1–S4† and are reported as an average of three reactions.

General procedure for performing pseudo-first-order reaction kinetics

Pseudo-first-order reaction conditions were used to establish the rate expression for the reaction between the POV-alkoxide clusters (**1-methyl** through **1-butyl**) and the H-atom transfer reagent, 5,10-dihydrophenazine. Using a UV-Vis-NIR spectrophotometer with temperature controls set to 25 °C, reactions between cluster and excess H$_2$Phen (13.3–16.7 equivalents) were tracked by monitoring the absorbance at 1025 nm over the reaction coordinate. Final reductant concentrations were varied from 8.0 to 10.0 mM, with a constant concentration of cluster of 0.60 mM. Samples of cluster stock solutions in MeCN were loaded in a long-necked quartz cuvette and sealed with a rubber septum before removing from the glovebox. In a 1 mL syringe, a sample of reductant stock solution (~35 mM in MeCN) was measured prior to removal from the glovebox. After equilibrating to 25 °C in the spectrophotometer, data acquisition began, and the reductant solution was forcefully injected to ensure efficient sample mixing. Upon the completion of the reaction, the plot of absorbance over time was fit to the following equation by least squares fitting:

$$A_t = A_{inf} + (A_0 - A_{inf})e^{-k_{obs} \times t}$$

where A_t is the absorbance at a given time, t, in seconds, A_{inf} is the absorbance at the end of the reaction (t = infinite), A_0 is the absorbance after reductant injection, and k_{obs} is the observed first order rate constant (s^{-1}). All reactions to determine k_{obs} were performed in triplicate. The good fit found for reaction curves indicated that the rate expression is first order with respect to reductant concentration (Fig. S3–S6†). Plotting k_{obs} as a function of reductant concentration generated a linear plot, meaning that the reaction rate expression is second order overall, such that:

$$\frac{d\left[V_6O_6(OR)_{12}{}^{1-}\right]}{dt} = k[H_2Phen]^1[V_6O_7(OR)_{12}{}^{1-}]^1$$

The slopes of the resultant k_{obs} *vs.* [H_2Phen] plots were normalized for the six possible reactive V=O sites on the cluster, as well as the two possible H-atoms which can be transferred from H_2Phen, in order to determine the second order rate constant, k_{PCET} (M^{-1} s^{-1}), such that:

$$k_{PCET} = \frac{\text{slope}}{6_{V=O} \times 2_{H\text{-atoms}}} = \frac{\text{slope}}{12}$$

Uncertainties were determined by performing a linear regression function on data from triplicate trials for each condition in Microsoft Excel and calculating a 95% confidence interval. With no observed induction period in the pseudo-first order kinetics traces, the y-intercept was held at the origin in all cases. The reported errors are the first significant figure of the difference between the determined slope and the confidence interval maximum.

To determine the deuterium kinetic isotope effect (KIE), analogous pseudo-first order reactions were performed under identical conditions, using the deuterium-labeled reductant species 5,10-dihydrophenazine-d_2 (D_2Phen) (Fig. S14–S17†). KIEs are found in Table 1. The prepared D_2Phen used for these reactions was found to be 91% D-labeled using ^{1}H NMR spectroscopy. We note that solvents used in kinetic analysis have been *rigorously* dried; residual water content of the acetonitrile was measured at 11 ppm.

General procedure for determining activation parameters for the reduction of $[V_6O_7(OR)_{12}]^{1-}$ *via* H-atom uptake

Eyring analysis was performed by collecting absorbance *vs.* time data at temperatures between 10 and 45 °C. Reactions were assembled in an analogous fashion to previously run experiments, with constant reductant and cluster concentrations of 8.0 and 0.60 mM and were run in triplicate (Fig. S18–S21†). Conversion of k_{obs} to k_{PCET} was done by dividing k_{obs} by the reductant concentration, and also by dividing by 12 to account for reaction probability. Plotting $\ln(k_{PCET}/T)$ as a function of $1/T$ (temperature converted in K), the linear plot was used to solve for activation parameters using the below equations where R is the gas constant in units of cal (mol^{-1} K^{-1}), k_{Boltz} is Boltzmann's constant, and h_{Planck} is Planck's constant, m is the slope, and b is the y-intercept.

$$\ln\left(\frac{k_{PCET}}{T}\right) = m \times \frac{1}{T} + b$$

$$\Delta H^{\ddagger} = m \times -R$$

$$\Delta S^{\ddagger} = R \times \left[b - \ln\left(\frac{k_{Boltz}}{h_{Planck}}\right)\right]$$

$$\Delta G^{\ddagger} = \Delta H^{\ddagger} - T\Delta S^{\ddagger}$$

Uncertainties were determined by performing a linear regression function on data from triplicate trials for each condition in Microsoft Excel and calculating a 95% confidence interval. The reported errors are the first significant figure of the difference between the confidence interval maximum and the values found from the regression.

Eyring plots and activation parameters are found in Fig. 5 and Table 1, respectively.

Table 1 Rate constants, kinetic isotope effects, and Eyring parameters describing H-atom uptake at POV-alkoxide clusters with variable surface ligand length in MeCN

Complex	k_{PCET}[a] (M^{-1} s^{-1})	KIE[a]	$\Delta H^{\ddagger}$ (kcal mol^{-1})	$\Delta S^{\ddagger}$ (cal mol^{-1} K^{-1})	$\Delta G^{\ddagger}$ (kcal mol^{-1})
1-methyl	0.45 ± 0.03	1.7	6.9 ± 0.7	−37.1 ± 2.3	17.9 ± 1.3
1-ethyl	0.020 ± 0.002	1.8	10.2 ± 1.3	−32.0 ± 4.2	19.7 ± 2.5
1-propyl	0.029 ± 0.002	1.9	9.5 ± 1.4	−33.7 ± 4.7	19.5 ± 2.8
1-butyl	0.022 ± 0.005	2.0	9.8 ± 1.3	−33.6 ± 4.5	19.8 ± 2.7

[a] At 25 °C.

Results and discussion

Previous work from our laboratory has demonstrated quantitative conversion of the fully-oxygenated, mono-anionic POV-methoxide cluster, $[V_6O_7(OCH_3)_{12}]^{1-}$ (**1-methyl**), to its oxygen-deficient congener $[V_6O_6(MeCN)(OMe)_{12}]^{1-}$ (**2-methyl**), following addition of an equivalent of 5,10-dihydrophenzine (H_2Phen) in acetonitrile.[38] Interested in interrogating structure–function relationships of O-atom vacancy formation at POV-alkoxide clusters featuring bridging alkoxide ligands of variable length, we set out to explore the scope of reactivity of $[V_6O_7(OR)_{12}]^{1-}$ (R = Et, ^{n}Pr, ^{n}Bu)[31,32] with H-atom transfer reagents. Initial experiments attempted the extension of O-atom defect formation *via* hydrogen atom transfer (HAT) to the POV-ethoxide cluster, $[V_6O_7(OEt)_{12}]^{1-}$ (**1-ethyl**).

Addition of 1 equiv. of H_2Phen to **1-ethyl** results in a colour change of the solution from green to red-pink over the course of 1 hour at room temperature. Analysis of the crude product by ^{1}H NMR spectroscopy reveals five paramagnetically shifted and broadened resonances, located at 29.87, 28.75, 1.24, 2.50 and −25.45 ppm (Fig. 2). The pattern of signals matches values reported previously by our group for the formation of the oxygen-deficient POV-ethoxide cluster, $[V_6O_6(MeCN)(OEt)_{12}]^{1-}$ (**2-ethyl;** Fig. 2).[41] Additionally, the anticipated byproducts of this reaction, phenazine and water, are also observed in the ^{1}H NMR spectrum of the reaction mixture.

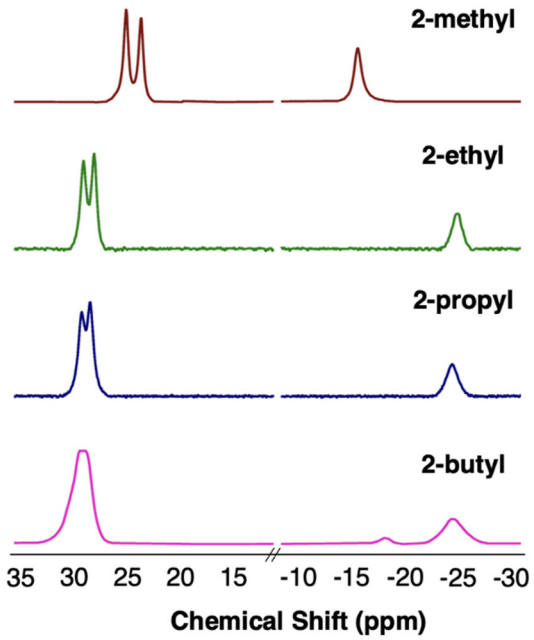

Fig. 2 ^{1}H NMR spectra of $[V_6O_6(MeCN)(OMe)_{12}]^{1-}$ (**2-methyl**; top, dark red), $[V_6O_6(MeCN)(OEt)_{12}]^{1-}$ (**2-ethyl**; middle, green), $[V_6O_6(MeCN)(O^nPr)_{12}]^{1-}$ (**2-propyl**; middle, blue) and $[V_6O_6(MeCN)(O^nBu)_{12}]^{1-}$ (**2-butyl**; bottom, magenta) collected in MeCN 21 °C. The diamagnetic region of the spectra has been omitted for clarity (see ESI file for full spectra†).

Following workup, **2-ethyl** was isolated as a brown powder in 89% yield (see Experimental section for details).

With successful formation of the O-atom deficient POV-ethoxide cluster *via* net H-atom uptake, we turned our attention to the reactivity of **1-propyl** and **1-butyl** with H_2Phen. Previous attempts to generate an O-atom vacancy at the surface of POV-alkoxide clusters functionalized with bridging alkoxide ligands with more than two carbons have failed, presumably due to the increased length of surface ligands blocking access to surface oxido ligands.[33] We hypothesized that the small size of an H-atom would facilitate activation of the V(v)=O bond required for defect formation. Indeed, addition of 1 equiv. of H_2Phen to **1-propyl** and **1-butyl** results in a gradual colour change from green to dark brown over the course of ~2 h. This observation is consistent with reduction of the cluster core, as intervalence charge transfer bands corresponding to electron transfer between V^{IV} and V^{V} centers available to the fully oxygenated POV-alkoxide cluster are quenched following reduction of the V(v) center to V(iii) and formation of the O-atom defect (Fig. S4†). The electronic absorption spectra of **2-propyl** and **2-butyl** resemble those reported for **2-methyl** and **2-ethyl**, with d → d transitions observed at 537 nm (ε = 164 M^{-1} cm^{-1}), 653 (ε = 98 M^{-1} cm^{-1}), and 1038 nm (ε = 184 M^{-1} cm^{-1}) for **2-propyl** and 535 nm (ε = 145 M^{-1} cm^{-1}), 655 nm (ε = 60 M^{-1} cm^{-1}), and 1061 nm (ε = 132 M^{-1} cm^{-1}) for **2-butyl**. The similarities in absorbance profiles suggest analogous distribution of vanadium ion oxidation states across the reduced assemblies ($V^{III}V^{IV}_5$).

Further evidence for the formation of **2-propyl** and **2-butyl** was obtained by analysis of the ^{1}H NMR spectra of the reaction mixtures; resonances assigned to the oxidized H-atom transfer reagent, phenazine, were observed, indicating successful H-atom transfer from the substrate to the cluster surface. Additionally, a series of paramagnetically broadened and shifted signals were observed (**2-propyl**: δ = 29.67, 28.89, −0.66, −2.18 and −24.88 pm; **2-butyl**: δ = 29.90, 29.10, 0.06 and −25.32 ppm), consistent with the formation of the O-atom deficient assembly. In the case of **2-butyl**, an additional signal was noted at −18.50 ppm; we assign this resonance to the protons of bridging methoxide ligands present at the surface of the cluster. This assignment is supported by the ESI-MS of the starting material, **1-butyl**, which shows a fraction of assemblies possessing bridging methoxide ligands as "impurities". Previous results from our laboratory have shown that the synthesis of the butoxide-substituted POV-alkoxide cluster reproducibly results in the formation of a complex featuring bridging methoxide ligands.[31] The O-atom deficient products were isolated as brown residues in good yield (**2-propyl**: 75%; **2-butyl**: 44%).

Following verification that O-atom defect formation is possible in the series of POV-alkoxide clusters *via* net H-atom uptake, we next investigated the consequences of varied bridging alkoxide ligand on the strength of O–H bonds formed along the reaction pathway. Such analyses provide insights into the reactivity of a given species with different substrates, expected reaction rates, and the role of electronic structure in the charge transfer process. The bond dissociation free energy (BDFE(E–H)) of a given element–hydrogen bond describes the free energy of homolytic bond cleavage, or the release of a hydrogen radical. This parameter is used to describe the thermodynamic driving force of a given net H-atom transfer reaction.[42]

The parent POV-alkoxide clusters studied in this work (**1-methyl**, **1-ethyl**, **1-propyl**, and **1-butyl**) feature the same oxidation state distribution of vanadium ions in the Lindqvist core ($V^{IV}_5V^{V}$) and similar reduction potentials (within 0.1 V).[31,32] As such, we hypothesized that the bond strength of the relevant terminal O–H's formed during PCET would be nearly identical. To determine the $BDFE(O–H)_{avg}$ for the terminal aquo moieties on the reduced-protonated complexes, we employed equilibrium analyses presented by Mayer.[43] In this approach, the exposure of a species of interest to an H-atom source which does not quantitatively transfer the reducing equivalents allows for the use of a modified version of the Nernst equation:

$$BDFE(E-H)_{adj} = BDFE(E-H) - \frac{1.364}{n}\log\left(\frac{[E-H]}{[E]}\right) \quad (1)$$

Where BDFE(E–H) is the BDFE of the H-atom transfer reagent, n is the number of H-atom equivalents transferred, and [E–H]/[E] is the ratio of reductant and its oxidized partner in solution at equilibrium. Subtraction of the relative concentration term from the known BDFE(E–H)produces the adjusted BDFE(E–H)

of the selected reagent after equilibration with the species of interest, which consequently equates to the BDFE(E–H) of the newly formed E–H bond.

Previous approximations of the BDFE(O–H)$_{avg}$ of the reduced-protonated form of $[V_6O_7(OCH_3)_{12}]^{1-}$ suggested a 61 kcal mol^{-1} bond strength; however, due to the non-equilibrium nature of the reactivity described in that publication (all reactivity performed in MeCN, resulting in dissociation of the water ligand from the reduced vanadium center), the reliability of this value is questionable.[38] More recently, our group has demonstrated reversible PCET to terminal V=O bonds at the surface of POV-alkoxide clusters; addition of H-atom transfer reagents to the vanadium oxide assemblies in tetrahydrofuran (THF), aquo-functionalized complexes can be accessed, allowing for the analysis of the thermodynamics of the PCET reaction at equilibrium.[30,44]

An additional requirement for obtaining equilibrium between the parent and reduced POV-alkoxide clusters is the use of a H-atom transfer reagent with a comparable BDFE(E–H) to that of the product, $[V_6O_6(OH_2)(OR)_{12}]^{1-}$ (R = Me, Et, ^{n}Pr, ^{n}Bu). Complete conversion to the reduced assemblies upon addition of H_2Phen (BDFE(N–H)$_{avg}$ = 59.2 kcal mol^{-1}) to $[V_6O_7(OR)_{12}]^{1-}$ indicates that a substrate with stronger E–H bonds is necessary. When the 2e$^-$/2H$^+$ donor hydrazobenzene (Hydz, BDFE(N–H)$_{avg}$ = 60.4 kcal mol^{-1})[42] was used as an alternative reductant, a mixture of organic and inorganic starting materials and products were observed, consistent with the desired equilibrium conditions for analysis of the BDFE(O–H)$_{avg}$ of the surface aquo ligand.

Reactions of 1 equivalent of reductant and cluster were run in triplicate for each complex in THF-d_8. After 7 days, the ^{1}H NMR spectra of reactions with **1-methyl** remain constant, indicating that the reaction reaches equilibrium in that time period (Fig. 3 and S5†). Using the established average bond strength of the two N–H bonds, an n value of 2, and the ratio of remaining Hydz and its oxidized partner, azobenzene (Azo), we determined the BDFE(O–H)$_{avg}$ for the aquo adduct of the O-atom deficient POV-alkoxide cluster **2-methyl** to be 59.9 ± 0.1 kcal mol^{-1} (Table S1†). The adjusted BDFEs calculated from reactions with the longer-chain complexes are slightly lower (**2-ethyl**: 59.7 ± 0.1 kcal mol^{-1}; **2-propyl**: 59.7 ± 0.1 kcal mol^{-1}; **2-butyl**: 59.7 ± 0.1 kcal mol^{-1}; Fig. 3 & S6–S8, Tables S2–S4†).

The experimentally determined BDFE(O–H)$_{avg}$ values for the aquo-bound variants of **2-methyl**, **2-ethyl**, **2-propyl**, and **2-butyl** are very similar, supporting our hypothesis that the length of the aliphatic surface ligand does not influence the driving force of H-atom uptake at the cluster surface. These results are broadly consistent with prior observations by our research team that the distribution of oxidation states across the Lindqvist core is the most important determinant of the strength of O–H bonds at the cluster surface.[30,38,45,46] Weakening of the O–H bond in water occurs as a result of its binding to the reduced vanadium center, a phenomenon known as coordination-induced bond weakening.[47] The degree of O–H bond activation is directly related to the electron density of the metal center to which water is bound; in the case of the O-atom deficient POV-alkoxide clusters, the V(III) ion which binds the aquo moiety is sensitive to the oxidation state distribution of surrounding metal centers composing the Lindqvist core. An exception to the dependence of H-atom affinity of the cluster surface solely on oxidation state distribution of vanadium ions was reported recently by our research group in the case of calix-[4]-arene-functionalized POV-alkoxide cluster, (calix)V_6O_6(MeCN)$(OMe)_{12}$.[44] In this example, the electron withdrawing nature of the multidentate, aryloxide ligand results in a depletion of electron density in the Lindqvist core, justifying the observation of a substantially stronger O–H bond for the aquo adduct of the POV-alkoxide cluster, (calix)$V_6O_5(OH_2)$(MeCN)$(OMe)_{12}$ (BDFE(O–H)$_{avg}$ = 62.4 ± 0.2 kcal mol^{-1}) in comparison to that of $[V_6O_5(OH_2)(MeCN)(OMe)_{12}]^0$ (BDFE(O–H)$_{avg}$ = 60.7 ± 0.1 kcal mol^{-1}), despite both complexes featuring a $V^{III}_2V^{IV}_4$ oxidation state distribution.[30,44]

In our initial experiments probing defect formation *via* PCET across the four POV-alkoxide clusters, we noticed a qualitative difference in time required for the reaction to reach completion. Specifically, the rate of reduction of **1-methyl** is significantly faster than that of the complexes bearing longer aliphatic chains. The analogous affinity of complexes **1-methyl**, **1-ethyl**, **1-propyl**, and **1-butyl** for H-atoms indicates that the

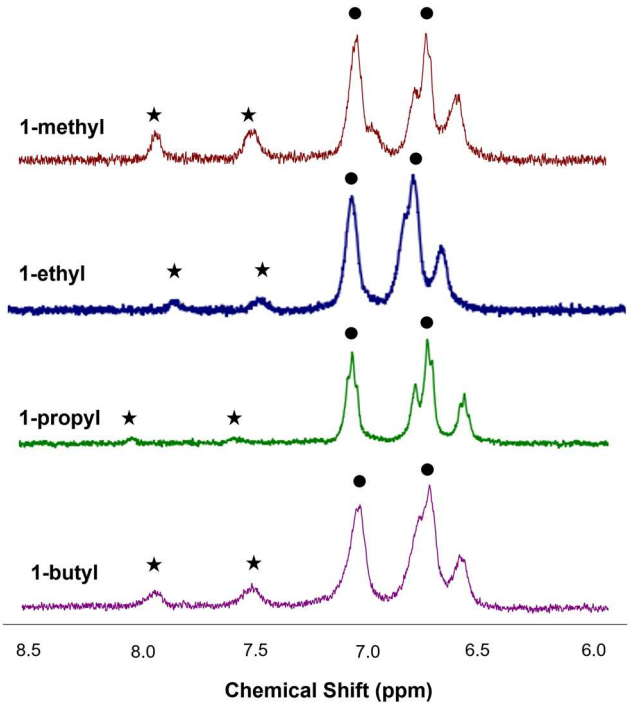

Fig. 3 ^{1}H NMR spectra from reactions of **1-methyl** (bottom, red), **1-ethyl** (blue), **1-propyl** (green), and **1-butyl** (magenta, top) with one equivalent of Hydz in THF-d_8 after 7 days, highlighting the presence of both azobenzene (Azo) and Hydz in solution. The signals used in calculations are labeled with asterisks (*) for Azo and solid dots (•) for Hydz. The ratio of these species at equilibrium was used to determine the BDFE(O–H)$_{avg}$ of the corresponding aquo moiety of **1-methyl** and **1-butyl** using eqn (1).

driving force for PCET to the cluster surface in all three examples is similar, suggesting that ligand length instead impacts the kinetics of H-atom uptake.

To gain insight into the role aliphatic surface groups play in dictating the kinetics of O-atom defect formation *via* H-atom uptake, we performed a series of kinetic analyses on these systems. We note that kinetics experiments were performed in acetonitrile (MeCN), which displaces the aquo moiety formed upon $2e^-/2H^+$ reduction. Despite the change in solvent between equilibrium and kinetics experiments, the BDFE(O–H)$_{avg}$ is not affected, as demonstrated by this parameter falling between 60 and 61 kcal mol^{-1} in both THF (60.3 kcal mol^{-1}, *vide supra*) and MeCN (found in benchmarking studies in a previous report from our group).[38] In general, BDFE values for organic and inorganic substrates are found to be similar in THF and MeCN, neutralizing any effect of reaction driving force on rate from this experimental change.[42]

First, we determined the rate expression for H-atom uptake at the surface of **1-ethyl**, **1-propyl**, and **1-butyl** to ensure consistent mechanisms of H-atom transfer. Electronic absorption spectroscopy was used to monitor the reduction of $[V_6O_7(OR)_{12}]^{1-}$ by H_2Phen under pseudo-first order reaction conditions at 25 °C (Fig. S9–S16†). We tracked the absorbance at 1025 nm as the electronic absorption spectra of all four parent POV-alkoxide clusters possess an intervalence charge transfer band at this wavelength that is quenched upon defect formation (Fig. S9, S11, S13 and S14†). The pseudo-first order rate constants (k_{obs}) of O-atom vacancy formation across a series of concentrations of H_2Phen was determined by fitting the change in absorption as a function of time to a second-order model (see Experimental section for details). When k_{obs} was plotted *versus* the concentration of reductant, a linear plot is observed (Fig. 4), indicating an identical rate expression for O-atom vacancy formation across all four POV-alkoxide clusters (eqn (2)).

$$\frac{d[V_6O_6(MeCN)]}{dt} = k[V_6O_7]^1[H_2Phen]^1 \quad (2)$$

The rate expression indicates the rate determining step involves a collision between reductant and cluster. This rate expression is consistent with previous reports from our laboratory probing the kinetics of O-atom vacancy formation at terminal V=O sites of POV-alkoxide clusters *via* PCET, suggesting that all POV-alkoxide clusters react *via* identical mechanisms.[30,38,44] Additional support for this hypothesis can be derived from the analogous KIE values measured for H-atom uptake in **1-propyl**, **1-ethyl**, **1-propyl**, and **1-butyl** (Fig. 4 and Fig. S17–S20†). The primary kinetic isotope effect indicates that the movement of a proton or H-atom is involved in the rate determining step of the reaction, as is suggested by the experimentally determined rate expression.

The slope of k_{obs} *vs.* [H_2Phen] allows for determination of the second-order rate constant (k_{PCET}) for H-atom uptake to complexes **1-methyl**, **1-ethyl**, **1-propyl**, and **1-butyl** (Fig. 4 and Table 1). For the formation of **2-methyl**, a k_{PCET} value of 0.45 ± 0.03 M^{-1} s^{-1} was obtained. This rate constant is greater than

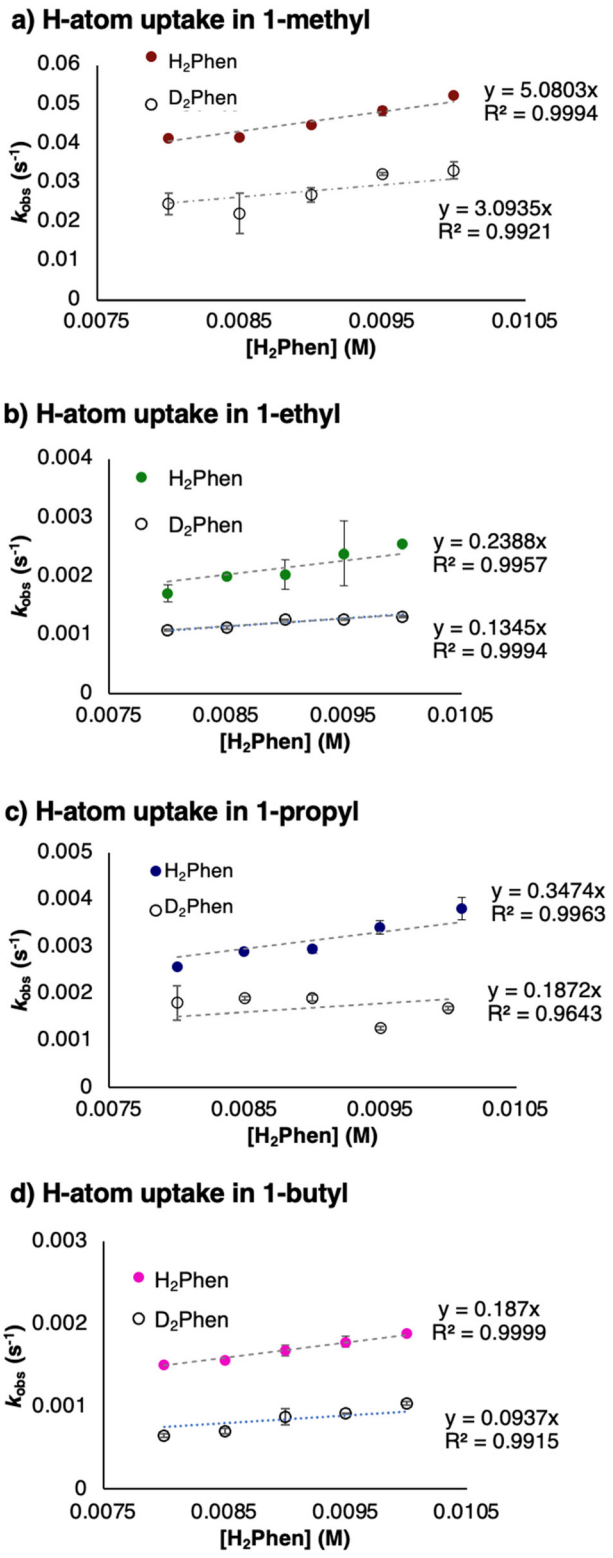

Fig. 4 Plot of k_{obs} as a function of [X_2Phen], where X = H, D. Concentration of cluster (**1-methyl**, top; **1-ethyl**, top–middle; **1-propyl**, bottom–middle; **1-butyl**, bottom) was held constant at 0.6 mM, and reductant concentration was varied between 8 mM and 10 mM (Fig. S17–S20†). Reactions were performed in MeCN. The slope of the resultant line provides the experimentally derived second-order rate constants, k_{PCET}. Linear regressions are calculated with a fixed intercept at the origin. Comparison of k_{PCET} for reactions with H_2Phen and D_2Phen provides KIE values for H-atom uptake at each cluster (Table 1).

that previously reported for this reaction using ^{1}H NMR to determine reaction rates (0.12 ± 0.03 M^{-1} s^{-1}).[38] We attribute this discrepancy to the method employed for each analysis. In the ^{1}H NMR method, samples of reductant and cluster were frozen in a J. Young tube to avoid premature mixing, and then thawed prior to analysis. However, upon thawing and placing into the spectrometer, some of the sample may have reacted, making it unclear how well the determined rates reflect the true initial rate of reaction. By performing kinetic analyses using absorption spectroscopy, the initial rate is easier to determine, as data is collected prior to and during reactant mixing. This allows for the earliest possible timepoints to be captured, improving accuracy of the fit.

Consistent with qualitative observations, the measured rate for the reduction of **1-methyl** is substantially faster than that observed for **2-ethyl** (k_{PCET} = 0.020 ± 0.002 M^{-1} s^{-1}), **2-propyl** (k_{PCET} = 0.029 ± 0.002 M^{-1} s^{-1}), and **2-butyl** (k_{PCET} = 0.022 ± 0.005 M^{-1} s^{-1}). These results suggest that the reactive vanadyl moiety in the methoxide-bridged assembly is less sterically shielded by its surface ligands in comparison to **1-ethyl**, **1-propyl**, and **1-butyl**. However, k_{PCET} for clusters bearing longer aliphatic ligands are all similar, suggesting a limitation to the effect of surface ligand size on reaction rates.

To probe the origin of the observed change in k_{PCET} between **1-methyl** and **1-ethyl**, we turned to variable temperature kinetic analyses (Fig. S21–S24†). Results from these experiments enable the determination of activation parameters through the construction of an Eyring plot, shedding light on the thermodynamics of the transition state involved in the PCET reaction. In these experiments, absorption at 1025 nm was monitored over the reaction coordinate at different temperatures (10 °C to 45 °C), while reactant concentrations were held constant (0.6 mM cluster, 8 mM H_2Phen).

As expected from our observations at 25 °C, the linear fit of the plot for **1-methyl** was distinguished from those with longer aliphatic groups and reflected disparate activation parameters (Fig. 5 and Table 1). The activation entropy ($\Delta S^{\ddagger}$ = −37.1 ± 2.3 cal mol^{-1} K^{-1}; Table 1) was found to be a large, negative value, analogous with previous results from our group which studied the rate of defect formation *via* H-atom uptake at **1-methyl** *via* ^{1}H NMR spectroscopy. This result suggests H-atom transfer proceeds *via* the formation of an ordered transition state, such as a hydrogen-bonded complex between a cluster and reductant pair. Additionally, the activation enthalpy ($\Delta H^{\ddagger}$ = 6.9 ± 0.7 kcal mol^{-1}; Table 1) was found to be relatively small in magnitude, indicating that the activation entropy plays a majority role in the rate limiting process, supporting an inner-sphere reaction. This observation is consistent with the reaction following a concerted proton–electron transfer (CPET) mechanism.[48,49]

The Eyring plots for surface activation of **1-ethyl**, **1-propyl**, and **1-butyl** are remarkably similar, producing consistent activation parameters describing the transition state of H-atom transfer to the POV-alkoxide surfaces (Table 1). Of note, $\Delta S^{\ddagger}$ for these reactions is ∼−33 cal mol^{-1} K^{-1}, representing a slight decrease in activation entropy *versus* **1-methyl**, while retaining

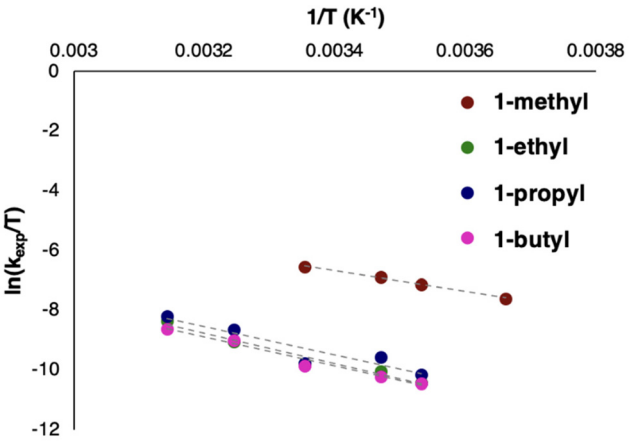

Fig. 5 Eyring plots for the reaction of **1-methyl** (red), **1-ethyl** (green), **1-propyl** (blue), and **1-butyl** (magenta) (0.6 mM) with H_2Phen 8 mM in MeCN between 10 °C and 45 °C (Fig. S21–S24†). *Y*-axis values were determined by dividing k_{obs} by the concentration of H_2Phen, providing the rate constant, k_{PCET}.

a substantial degree of organization for the transition state. In addition, the activation enthalpies of these bulkier complexes are found to be significantly higher than that of **1-methyl** ($\Delta H^{\ddagger}$ ∼ 10 kcal mol^{-1}, Table 1). This suggests a greater energetic requirement to access the purported H-bonded intermediate. Overall, these results show a ∼2 kcal mol^{-1} increase in Gibbs Free Energy of activation, $\Delta G^{\ddagger}$, consistent with the 20-fold decrease in reaction rate observed from **1-methyl** to its long-chain congeners. Similar magnitudes of rate change with respect to the change in activation energy is consistent with previous reporting from our group, wherein a difference in $\Delta G^{\ddagger}$ of about 4 kcal mol^{-1} for PCET between an oxygenated and O-atom deficient cluster was shown to correspond with a 100-fold difference in rate.[30]

Despite the reduction in entropic contributions to $\Delta G^{\ddagger}$ for reduction of the bulkier clusters, these parameters are still indicative of a CPET process, meaning that the steric encumbrance introduced by modification of the surface ligand length does not affect the overall reaction mechanism. However, surface ligands do impact the transition state thermodynamics despite their minimal influence on overall driving force. For example, the decrease in magnitude of $\Delta S^{\ddagger}$ for the activation of **1-ethyl** *versus* **1-methyl**, and therefore reduction in transition state ordering, is an expected result, as the additional –CH_2– link should serve to lengthen the O–H–N interaction in the activated complex. This is anticipated to slow the rate of PCET by increasing the distance which H-atom equivalents must travel during the net H-atom transfer reaction. In addition, the significant increase in $\Delta H^{\ddagger}$ is also a consequence of the steric bulk of surface groups. The degrees of freedom of the aliphatic chains can theoretically produce a number of structures which inhibit H_2Phen from making van der Waals contact with the V=O site, preventing access to the transition state required for H-atom transfer. Rearrangement of the ligand shell orientation exposes the oxo terminus, allowing for

interactions between cluster and reductant and resulting in productive reactivity. Surface rearrangement is expected to play a significant role in the increased enthalpic contribution to the activation barrier. Ligand shell rearrangement is less relevant for **1-methyl** to react, as the single carbon-long organic ligand is not expected to inhibit H_2Phen binding, reflected in its relatively small value for $\Delta H^{\ddagger}$.

As stated above, our results indicate that both k_{PCET} and the activation parameters of H-atom uptake at **1-ethyl**, **1-propyl**, and **1-butyl** are similar. This result is surprising, as we had originally hypothesized that the increased number of $-CH_2-$ chain links would impart further steric protection of the terminal vanadyl moieties. In hindsight, we can justify the similar H-atom transfer kinetics through the poor compatibility of the aliphatic surface moieties and solvent in which reactions are run (MeCN). Previous work from our laboratory describes the diffusion coefficients for $[V_6O_7(OR)_{12}]^0$ (R = C_2H_5, C_3H_7, C_4H_9, C_5H_{11}) clusters in MeCN ($\sim 10^{-6}$–10^{-5} cm^2 s^{-1}); despite an increase in molecular weight and anticipated cluster diameter, diffusion coefficients for all POV-alkoxide clusters resemble one another.[31,32] This observation suggests that the aliphatic ligands are "pinned" to the surface of the assembly, collapsing in on themselves to avoid extensive interactions with acetonitrile. This manifests in analogous diffusion coefficients despite apparent increases in size. In other words, solvent incompatibility of the nonpolar alkoxide ligands may limit the possible orientations available to surface groups beyond $-OC_2H_5$ in length. We hypothesize that this trait of the long-chain POV-alkoxide clusters (*e.g.* **1-ethyl**, **1-propyl**, **1-butyl**) in MeCN results in clusters structures with similar V=O site accessibility. Given that all terminal vanadyl moieties are chemically equivalent in the parent POV-alkoxide clusters, reactivity can be isolated to a single, solvent-exposed site. Thus, the O–H–N distance and geometry would be expected to be relatively unchanged for complexes featuring surface ligand lengths beyond two carbons, resulting in similar values for $\Delta S^{\ddagger}$, as is observed experimentally. This also prevents changes to $\Delta H^{\ddagger}$ beyond **1-ethyl** by leveraging core electron delocalization to minimize energy penalties associated with ligand rearrangement and maintain similar probabilities of productive cluster-reductant collisions.

Conclusion

Atomic-level insights into the physicochemical properties of nanocrystalline oxides and their reactivities toward H-atom equivalents are important for the development of active materials for efficient, surface-mediated PCET processes. To better understand the role which surface ligands play in charge transfer at the surface of materials, we employ a series of isostructural/isoelectronic Lindqvist-type POV-alkoxide clusters ($[V_6O_7(OR)_{12}]^{1-}$) which feature different-length pendant ligands (R = CH_3 through C_4H_9). All four complexes are shown to be active toward net H-atom uptake to the lone V^V=O moiety on the cluster surface, with their similar core properties resulting in analogous H-atom binding thermodynamics, represented by the similar $BDFE_{avg}$(O–H)s found for the corresponding H-atom installed species, $[V_6O_6(OH_2)(OR)_{12}]^{1-}$.

Despite conserved reaction driving force across the series, the methoxide-functionalized complex (**1-methyl**) was found to react ~20× faster than its long-chain analogues with the same reductant, indicating a significant steric influence imparted by surface sterics. Interestingly, the longer-chain derivatives (**1-propyl** and **1-butyl**) were found to react at analogous rates to that of **1-ethyl**. We find this to be a consequence of the increased conformational degrees of freedom afforded to these surface ligands on the cluster, buffering further steric influence on reaction rates through dynamic changes in chain conformation and solvation in MeCN. These results highlight several influences imparted by capping ligands on surface-mediated processes at nanoparticles, providing a design handle to decouple and tune reaction rates and selectivity without altering thermodynamics.

Author contributions

C. Y. M. P., E. S., and E. M. M. conceived all experiments. C. Y. M. P. and E. S. performed the synthesis and characterization of all complexes, and collected experimental data of relevance to kinetic measurements. K. R. P. performed equilibrium reactions and scanning kinetics experiments. All authors contributed to the writing of the manuscript.

Conflicts of interest

There are no conflicts to declare.

Acknowledgements

This research was funded by the National Science Foundation (CHE-2154727). E. S. is a recipient of the Messersmith Fellowship from the University of Rochester which has provided support for this study.

References

1 E. Pomerantseva, F. Bonaccorso, X. Feng, Y. Cui and Y. Gogotsi, *Science*, 2019, **366**, eaan8285.
2 Y. Li, S. Xiao, T. Qiu, X. Lang, H. Tan, Y. Wang and Y. Li, *Energy Storage Mater.*, 2022, **45**, 741–767.
3 Z.-Y. Zhou, N. Tian, J.-T. Li, I. Broadwell and S.-G. Sun, *Chem. Soc. Rev.*, 2011, **40**, 4167–4185.
4 M. Fernández-García, A. Martínez-Arias, J. C. Hanson and J. A. Rodriguez, *Chem. Rev.*, 2004, **104**, 4063–4104.
5 G. Cotin, C. Blanco-Andujar, F. Perton, L. Asín, J. M. de la Fuente, W. Reichardt, D. Schaffner, D.-V. Ngyen, D. Mertz, C. Kiefer, F. Meyer, S. Spassov, O. Ersen, M. Chatzidakis, G. A. Botton, C. Hénoumont, S. Laurent, J.-M. Greneche,

F. J. Teran, D. Ortega, D. Felder-Flesch and S. Begin-Colin, *Nanoscale*, 2021, **13**, 14552–14571.
6 R. M. Hewlett and M. A. McLachlan, *Adv. Mater.*, 2016, **28**, 3893–3921.
7 J. J. Calvin, A. S. Brewer and A. P. Alivisatos, *Nat. Synth.*, 2022, **1**, 127–137.
8 A. Heuer-Jungemann, N. Feliu, I. Bakaimi, M. Hamaly, A. Alkilany, I. Chakraborty, A. Masood, M. F. Casula, A. Kostopoulou, E. Oh, K. Susumu, M. H. Stewart, I. L. Medintz, E. Stratakis, W. J. Parak and A. G. Kanaras, *Chem. Rev.*, 2019, **119**, 4819–4880.
9 K. E. Knowles, M. Tagliazucchi, M. Malicki, N. K. Swenson and E. A. Weiss, *J. Phys. Chem. C*, 2013, **117**, 15849–15857.
10 R. Hayoun, K. M. Whitaker, D. R. Gamelin and J. M. Mayer, *J. Am. Chem. Soc.*, 2011, **133**, 4228–4231.
11 J. N. Schrauben, R. Hayoun, C. N. Valdez, M. Braten, L. Fridley and J. M. Mayer, *Science*, 2012, **336**, 1298–1301.
12 R. G. Agarwal and J. M. Mayer, *J. Am. Chem. Soc.*, 2022, **144**, 20699–20709.
13 J. L. Peper and J. M. Mayer, *ACS Energy Lett.*, 2019, **4**, 866–872.
14 J. W. Darcy, B. Koronkiewicz, G. A. Parada and J. M. Mayer, *Acc. Chem. Res.*, 2018, **51**, 2391–2399.
15 J. Castillo-Lora, M. F. Delley, S. M. Laga and J. M. Mayer, *J. Phys. Chem. Lett.*, 2020, **11**, 7687–7691.
16 S. M. Laga, T. M. Townsend, A. R. O'Connor and J. M. Mayer, *Inorg. Chem. Front.*, 2020, **7**, 1386–1393.
17 M. T. Pope and A. Müller, *Angew. Chem., Int. Ed. Engl.*, 1991, **30**, 34–48.
18 D. L. Long, R. Tsunashima and L. Cronin, *Angew. Chem., Int. Ed.*, 2010, **49**, 1736–1758.
19 Y.-F. Song and R. Tsunashima, *Chem. Soc. Rev.*, 2012, **41**, 7384–7402.
20 B. E. Petel and E. M. Matson, *Chem. Commun.*, 2020, **56**, 13477–13490.
21 K. R. Proe, E. Schreiber and E. M. Matson, *Acc. Chem. Res.*, 2023, **56**, 1602–1612.
22 P. Gouzerh and A. Proust, *Chem. Rev.*, 1998, **98**, 77–112.
23 A. Dolbecq, E. Dumas, C. R. Mayer and P. Mialane, *Chem. Rev.*, 2010, **110**, 6009–6048.
24 Y.-F. Song, D.-L. Long, C. Ritchie and L. Cronin, *Chem. Rec.*, 2011, **11**, 158–171.
25 J. Zhang, Y. Huang, G. Li and Y. Wei, *Coord. Chem. Rev.*, 2019, **378**, 395–414.
26 S. Chakraborty, B. E. Petel, E. Schreiber and E. M. Matson, *Nanoscale Adv.*, 2021, **3**, 1293–1318.
27 X. López, C. Bo and J. M. Poblet, *J. Am. Chem. Soc.*, 2002, **124**, 12574–12582.
28 J. Li, I. Huth, L.-M. Chamoreau, B. Hasenknopf, E. Lacôte, S. Thorimbert and M. Malacria, *Angew. Chem., Int. Ed.*, 2009, **48**, 2035–2038.
29 E. Schreiber, W. W. Brennessel and E. M. Matson, *Chem. Sci.*, 2023, **14**, 1386–1396.
30 S. E. Cooney, E. Schreiber, W. W. Brennessel and E. M. Matson, *Inorg. Chem. Front.*, 2023, **10**, 2754–2765.
31 A. M. Kosswattaarachchi, L. E. VanGelder, O. Nachtigall, J. P. Hazelnis, W. W. Brennessel, E. M. Matson and T. R. Cook, *J. Electrochem. Soc.*, 2019, **166**, A464.
32 L. E. VanGelder, E. Schreiber and E. M. Matson, *J. Mater. Chem. A*, 2019, **7**, 4893–4902.
33 B. E. Petel, R. L. Meyer, W. W. Brennessel and E. M. Matson, *Chem. Sci.*, 2019, **10**, 8035–8045.
34 E. Schreiber, N. A. Hartley, W. W. Brennessel, T. R. Cook, J. R. McKone and E. M. Matson, *ACS Appl. Energy Mater.*, 2019, **2**, 8985–8993.
35 R. E. Garwick, E. Schreiber, W. W. Brennessel, J. R. McKone and E. M. Matson, *J. Mater. Chem. A*, 2022, **10**, 12070–12078.
36 C. Daniel and H. Hartl, *J. Am. Chem. Soc.*, 2005, **127**, 13978–13987.
37 J. Lee, K. Shizu, H. Tanaka, H. Nakanotani, T. Yasuda, H. Kaji and C. Adachi, *J. Mater. Chem. C*, 2015, **3**, 2175–2181.
38 E. Schreiber, A. A. Fertig, W. W. Brennessel and E. M. Matson, *J. Am. Chem. Soc.*, 2022, **144**, 5029–5041.
39 G. R. Fulmer, A. J. M. Miller, N. H. Sherden, H. E. Gottlieb, A. Nudelman, B. M. Stoltz, J. E. Bercaw and K. I. Goldberg, *Organometallics*, 2010, **29**, 2176–2179.
40 E. Schreiber, W. W. Brennessel and E. M. Matson, *Inorg. Chem.*, 2022, **61**, 4789–4800.
41 E. Schreiber, B. E. Petel and E. M. Matson, *J. Am. Chem. Soc.*, 2020, **142**, 9915–9919.
42 R. G. Agarwal, S. C. Coste, B. D. Groff, A. M. Heuer, H. Noh, G. A. Parada, C. F. Wise, E. M. Nichols, J. J. Warren and J. M. Mayer, *Chem. Rev.*, 2022, **122**, 1–49.
43 R. G. Agarwal, H.-J. Kim and J. M. Mayer, *J. Am. Chem. Soc.*, 2021, **143**, 2896–2907.
44 S. E. Cooney, A. A. Fertig, M. R. Buisch, W. W. Brennessel and E. M. Matson, *Chem. Sci.*, 2022, **13**, 12726–12737.
45 A. A. Fertig, W. W. Brennessel, J. R. McKone and E. M. Matson, *J. Am. Chem. Soc.*, 2021, **143**, 15756–15768.
46 A. A. Fertig and E. M. Matson, *Inorg. Chem.*, 2023, **62**, 1958–1967.
47 N. G. Boekell and R. A. Flowers II, *Chem. Rev.*, 2022, **122**, 13447–13477.
48 T. G. Carrell, P. F. Smith, J. Dennes and G. C. Dismukes, *Phys. Chem. Chem. Phys.*, 2014, **16**, 11843–11847.
49 N. Kindermann, C.-J. Günes, S. Dechert and F. Meyer, *J. Am. Chem. Soc.*, 2017, **139**, 9831–9834.